Auxiliary material for:

Salt marsh–atmosphere exchange of energy, water vapor, and carbon dioxide: Effects of tidal flooding and biophysical controls

Kevan B. Moffett[1], Adam Wolf[2], Joe A. Berry[2], and Steven M. Gorelick[1]

[1] Department of Environmental Earth System Science, Stanford University, Stanford, CA, USA.
[2] Department of Global Ecology, Carnegie Institution for Science, Stanford, CA, USA.

This manuscript supplement provides additional detail on the methods, analysis, and results of the study.

The contents of this supplement are:

1. Eddy flux data processing and turbulent cospectra quality.
2. Soil heat flux and change in water heat storage calculations: comparison of methods.
3. Energy balance closure analysis.
4. Plant leaf gas flux measurements and details of leaf metabolism model.
5. Detailed flux model results and correlations between pre- and post- calibration model results and field data.
6. References cited in this supplement.

1. Eddy flux data processing and turbulent cospectra quality

Fluxes of CO_2, water, heat, and momentum were measured at the salt marsh field site using an eddy flux (EF) system based on a fast-response open-path infrared gas analyzer (IRGA; model LI-7500, Licor, Inc. Lincoln, NE) coupled with a 3-dimensional sonic anemometer (model CSAT-3, Campbell Scientific, Logan, UT), both installed at 2.14 m above the marsh surface. Digital signals from these instruments were recorded at 10 Hz using a Campbell Scientific CS5000 datalogger. All raw data were archived for later post-processing.

Data were processed in several steps to compute either fluxes or cospectra. The steps in flux processing were:

1) parsing data into 30 minute intervals;
2) recursively removing spikes greater than 6 σ beyond a quadratic fit to the 10 Hz data;
3) rotation to a natural coordinate system [Lee et al., 2004];
4) removing signal asynchrony by maximizing the magnitude of covariance between each scalar and the vertical wind [e.g., Eugster et al., 1997];
5) calculating scalar fluxes using the mean and covariance of each scalar with the vertical wind;
6) making frequency domain corrections to the fluxes for path-length averaging using the filter coefficients summarized in Massman [2000]; and
7) adjusting fluxes for air density artifacts [Webb et al., 1980].
8) Turbulent fluxes (*H* and *LE*) were rescaled to balance the energy budget, while preserving the Bowen ratio (β = *H/LE*), discussed in more detail below.

Calculation of power spectra and cospectra was identical for steps 1-5, after which:

5b) power spectra and cospectra were calculated and aggregated into 24 frequency bins; and
6b) cospectra for each scalar (denoted generically X below) were divided by the transfer function H_x for each frequency bin (f), using filter coefficients (τ) for each instrument's sensor separation distance:

$$\tau_{wC,wQ} = \sqrt{\tau_{IRGA}^2 + \tau_{CSAT_Z}^2} \quad \text{(S1)}$$

$$\tau_{wU} = \sqrt{\tau_{CSAT_Z}^2 + \tau_{CSAT_{XY}}^2} \quad \text{(S2)}$$

$$\tau_{wT} = \sqrt{\tau^2_{CSAT_Z}} \quad \text{(S3)}$$

$$H_x^{-1}(f) = 1 + (2\pi f \tau_{wx})^2 \quad \text{(S4)}$$

$$Co(wX)' = Co(wX) / H_x \quad \text{(S5)}$$

where *Co(wX)* refers to the cospectrum of *wX*, where *w* is the vertical wind and *X* is a generic scalar (e.g., *U* for streamwise horizontal wind, *T* for temperature, *Q* for H_2O_v, and *C* for CO_2). The subscripts to τ refer to the instruments used to measure the scalars, including an infrared gas analyzer (IRGA) for CO_2 and H_2O_v, and a sonic anemometer (CSAT) for horizontal (*x*) and vertical (*z*) components of the wind.

7b) Finally, the frequencies were transformed into the dimensionless frequency $\eta = fz/U$, and each cospectrum divided by its corresponding flux.

The cospectra of the turbulent fluxes showed that the data quality is high from the perspective of capturing all the scales of turbulent exchange (Figure S1). The shape and location of the cospectral peak for different stability regimes are consistent with expectations: unstable conditions have a broader cospectrum, with a lower frequency peak, stable conditions have a narrower cospectrum with a higher frequency peak, and neutral stability conditions are intermediate.

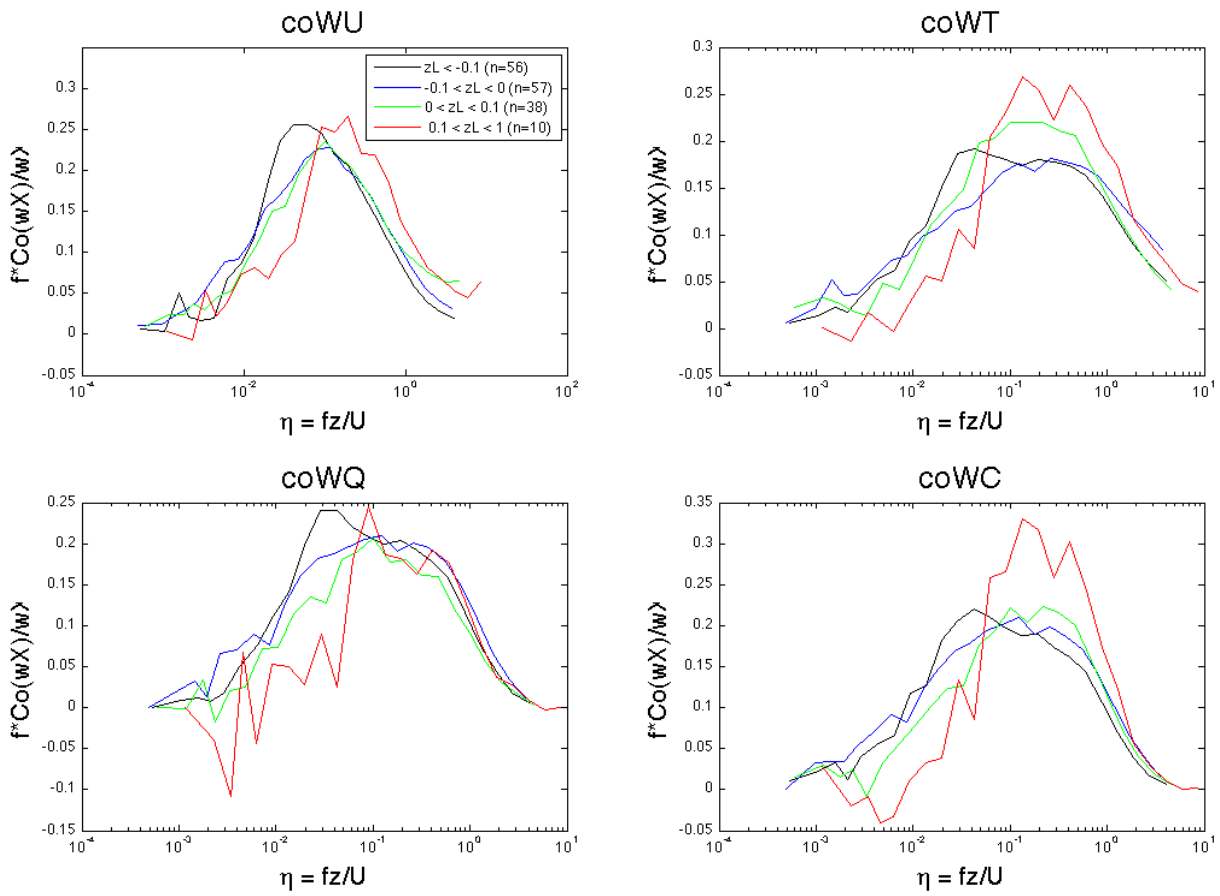

Figure S1. Cospectra of vertical wind with streamwise horizontal wind (coWU), air temperature (coWT), water vapor flux (coWQ), and carbon dioxide flux (coWC). Y-axes are cospectrum values divided by scalar flux magnitude. X-axes are dimensionless frequencies. Each colored line corresponds to data from a different stability regime, as per the stability parameter zL in the legend. The shapes of the turbulent flux cospectra, including both high and low frequency tails, indicate high data quality from the perspective of capturing all the scales of turbulent exchange.

2. Soil heat flux and change in water heat storage calculations: comparison of methods

In studies of ecosystem surface energy balance the magnitude of the ground heat flux is often uncertain. We expected that changes in the ground heat flux would account for a significant portion of the change in the salt marsh energy balance during flood events, so we sought to constrain this flux carefully. To do so, we conducted multiple independent calculations of the two components of this flux: soil heat flux and change in surface water heat storage. We calculated the soil heat flux: 1) from heat flux plate data and 2) from temporal changes in soil temperature profiles. We calculated the change in surface water heat storage: 1) from temporal changes in surface water temperature profiles, 2) from the change in the average surface water temperature, 3) from the residual of the flood water energy balance, accounting for the re-radiation of long wave energy from the water surface and estimating the latent and sensible heat fluxes from the water surface using bulk aerodynamic models of turbulent energy transport, and 4) as the residual of the marsh surface energy balance measured during flooding events. For simplicity, the heat flux plate and residual methods were included in the manuscript. For completeness, all methods are discussed here.

The data supporting these ground heat flux calculations were: thirty-minute averages of soil temperature and heat flux recorded at the eddy flux (EF) tower location [Campbell TCAV, HFT3, HFP01SC, CS616], six soil temperature profiles of eight points each, from 1 to 50 cm depth, recorded every 10 minutes near the EF tower [iButton DS1922L], and two surface water temperature profiles recorded near the EF tower every 10 minutes by means of 11 pairs of loggers attached every 10-cm along a 1-m-long plastic pipe [Onset HOBO WaterTempPro v1], secured to the ground at one end, and fitted with flotation bottles at the other end. Tidal stage, temperature, and salinity were recorded every 10 minutes at the base of the EF tower and at three locations in the primary tidal channels [Odyssey Pressure/Temperature, Conductivity/Temperature data recorders].

Soil heat flux

1) Our first estimate of soil heat flux (G_s) used the standard heat flux plate method (S6). This method combines a heat flux plate-measured soil heat flux (F_H, average of four

measurements) at some depth (d) with the change in heat storage in the overlying soil medium (ΔS_s).

$$G_s = F_H + \Delta S_s = F_H + \left(c_s \cdot \Delta T_s \cdot d\right)/\Delta t = F_H + \left(\rho_b c_d + \theta \rho_{sw} c_w\right) \cdot \left(\Delta T_s \cdot d\right)/\Delta t \quad \text{(S6)}$$

2) Our second estimate of soil heat flux was calculated from the average of the six soil temperature profiles as: the sum of the changes in heat storage (ΔS_s) for each soil layer plus the deep heat conduction between bottom of the profile and a constant temperature measured at the bottom of a nearby well (S7). ΔS_s was calculated as in the previous method.

$$G_s = \sum_{i=1}^{8} \left(\Delta S_s\right)_i + k\left(T_b - T_d\right)/\Delta z \quad \text{(S7)}$$

Change in surface water heat storage

1) Our first estimate of the change in surface water heat storage was calculated from the average of the two surface water temperature profiles using a change-in-storage method analogous to that used to calculate soil heat flux (S8).

$$G_w = \sum_{i=1}^{11} \left(\Delta S_w\right)_i = \sum_{i=1}^{11} \left(\rho_{sw} \cdot c_w \cdot \Delta T_{wi} \cdot d/\Delta t\right)_i \quad \text{(S8)}$$

2) Our second estimate of water heat flux was the average change in surface water heat storage ($\overline{\Delta S_w}$) calculated as in the previous method, but using the average temperature of the profile ($\overline{\Delta T_w}$) and the total flood water depth (d_{total}) (S9). This method is comparable to using a point-measurement of surface water temperature to calculate the change in surface water heat storage, as is commonly done in other studies accounting for surface water heat storage.

$$G_w = \overline{\Delta S_w} = \rho_{sw} \cdot c_w \cdot \overline{\Delta T_w} \cdot d_{total}/\Delta t \quad \text{(S9)}$$

3) Our third estimate of water heat flux was the residual of the flood water energy balance. In this energy balance we accounted for the reradiation of longwave energy from the water surface and estimated the latent (λE_w) and sensible (H_w) heat fluxes from the water surface using bulk aerodynamic models of turbulent energy transport (S10). We used the soil heat flux (G_s) from the heat flux plate method (S6). We used temperature measured at the top of the surface water temperature profile for the water surface temperature (T_w).

$$G_w = R_n - G_s - H_w - \lambda E_w \quad \text{(S10a)}$$

$$G_w = \left((1-\alpha)\cdot S_d + L_d - \varepsilon\cdot\sigma\cdot T_{ws}^4\right) - G_s - \frac{\rho_a\cdot c_p\cdot\left(T_{ws}-T_a\right)}{r_{aw}} - \frac{\rho_a\cdot c_p\cdot\left(e_{Tw}^{*}-e_a\right)}{\gamma\cdot\left(r_{aw}+r_{sw}\right)} \quad \text{(S10b)}$$

4) Our fourth estimate of water heat flux was the residual of the measured marsh surface energy balance during flooding events (S11). The energy balance was based on the measured net radiation (R_n), soil heat flux (G_s, from (S6)), sensible heat flux (eddy flux H), and latent heat flux (eddy flux λE).

$$G_w = R_n - G_s - H_{EF} - \lambda E_{EF} \quad \text{(S11)}$$

Method comparison

The soil heat flux plate method produced reliable data even in the intermittently flooded salt marsh system. Soil temperature profiles appeared to suffer from incomplete seals with the surrounding material: their signal was apparently damped by macropore convection around the sensors and were not suitable for calculating G_s. The magnitude of the soil heat flux (G_s) calculated using the soil temperature profile method exhibited very large changes at the onset of flooding. This anomaly suggested that the temperature profile stakes were not sufficiently sealed to surrounding sediments and acted as macropores. Water surrounding the sensors would account for the observed damping of the heat flux signal, highlighting a methodological issue in measuring ground heat flux during flood events. The magnitude of G_s calculated using the temperature profile method was 52% of that calculated using the heat flux plate method, on average. In contrast, G_s data calculated using the heat flux plate method nearly matched the net radiation during non-flooded periods at night (when the energy balance was $R_n \approx G_s$). During non-flooded mid-day periods, the soil heat flux (G_s) was approximately 17% of net radiation (R_n). On average, over all recorded times, the soil heat flux (G_s) was approximately 36% of net radiation (R_n).

The common method of calculating G_w from the change in standing water temperature did not work well in the salt marsh environment because of the short duration of standing water and significant surface water advection. The most precise method of closing the surface energy balance at our site was, unsurprisingly, the residual calculation (S11). In the absence of a measured energy balance, and based only on easily-measured meteorological data, the best estimate of G_w for our intertidal salt marsh environment resulted from the calculation (S10).

The net heat storage of flood waters increased during daytime floods and decreased at night by comparable orders of magnitude. The estimates of G_w using measured surface water temperatures and the water energy balance method suffered from large heat flux anomalies of the wrong sign during the onset of flooding. We attribute this error to the lag time required for the temperature sensing instruments to equilibrate to the flood water temperature: the effect was less prominent in the water energy balance method, which was less reliant on temperature data. We removed these anomalies by setting them to zero resulting in a conservative estimate of the duration of the effects of G_w.

Values of G_w calculated directly from changes in surface water temperature (S8 and S9) were of large peak magnitude (+265 to 832 W/m^2, daytime; -593 to -1319 W/m^2, night-time) and occurred over very short time periods during flooding. In contrast, G_w calculated using the water energy balance method (S10) occurred more gradually throughout the flood and reached lower peak magnitudes (+404 to 528 W/m^2, daytime; -201 to 252 W/m^2, night-time). The values of G_w calculated as the residual of the measured marsh surface energy balance during flooded intervals (S11) were lower yet (+204 to 337 W/m^2, daytime; -140 to 188 W/m^2, night-time). Where possible the estimation of G_w as the residual of a measured energy balance (S11) is likely to provide the best results. Estimation of G_w by a surface water energy balance if the water surface temperature is known (S10) is a better substitute method than calculation of G_w directly from slow-responding surface water temperature loggers (S8 and S9), but is still likely to over-estimate G_w. On average, over day and night tides, G_w (residual method) was about 8% of R_n.

3. Energy balance closure analysis

The physics of the salt marsh surface energy balance requires that the total available energy (AE), the net radiation (R_n) less soil heat flux (G_s) and change in surface water heat storage (ΔS_w), be completely balanced by the turbulent dissipation of energy by the sensible (H) and latent (λE) heat fluxes (S12).

$$AE = R_n - G_s - \Delta S_w = H + \lambda E \quad \text{(S12)}$$

One means of evaluating energy balance closure is the net residual error (ε):

$$|\varepsilon| = |R_n - G_s - \Delta S_w - H - \lambda E| \quad \text{(S13)}$$

The energy balance closure of daytime turbulent fluxes was fairly low over all (~49%, Figure S2a). Energy balance is notoriously difficult to achieve adjacent to water bodies because the strong difference in surface temperatures between water and land creates differences in buoyancy, hence vertical wind-speed over the two surfaces, that is balanced by advection, i.e., a sea-breeze effect. This is seen in the strong diurnal cycle in energy balance closure, in which closure is substantially higher in the morning than the afternoon, with a transition around midday. The presence of the advection compromises the assumption that the flux can be estimated as a 1-D (vertical) process. Nevertheless, the quality of the cospectra suggest that the measurements do capture the turbulent exchange that is at the heart of the eddy flux technique, but that the measurements under-represent the fluxes due to the presence of advection. Therefore, the energy balance of the entire suite of data was adjusted by rescaling the latent (λE) and sensible (H) heat fluxes by a single factor, estimated from mid-day non-flooded conditions, which achieved overall energy balance closure while preserving the Bowen ratio of the fluxes, after [Twine et al., 2000].

The absence of an estimate for the change in surface water heat storage (ΔS_w) in the eddy flux data during flood events also contributed to the failure to close the energy balance. Calibrating the values of ΔS_w according to the energy balance residual during flood events eliminated this discrepancy. The improvements in the energy balance by applying the method of Twine et al. [2000] and accounting for the change in surface water heat storage are shown in Table S1 and Figure S2.

Table S1. Evaluation of energy balance closure. ε and b in (W/m^2); D and a unitless.	
Closure method	$\lvert\varepsilon\rvert$ median
Daytime	
raw H and λE eddy flux data	143
H and λE scaled by 1.8, $\Delta S_w = 0$	1.87
scaled H and λE with ΔS_w from residual	0
Nighttime	
raw H and λE eddy flux data	6.11
H and λE scaled by 1.8, $\Delta S_w = 0$	4.70
scaled H and λE with ΔS_w from residual	2.69

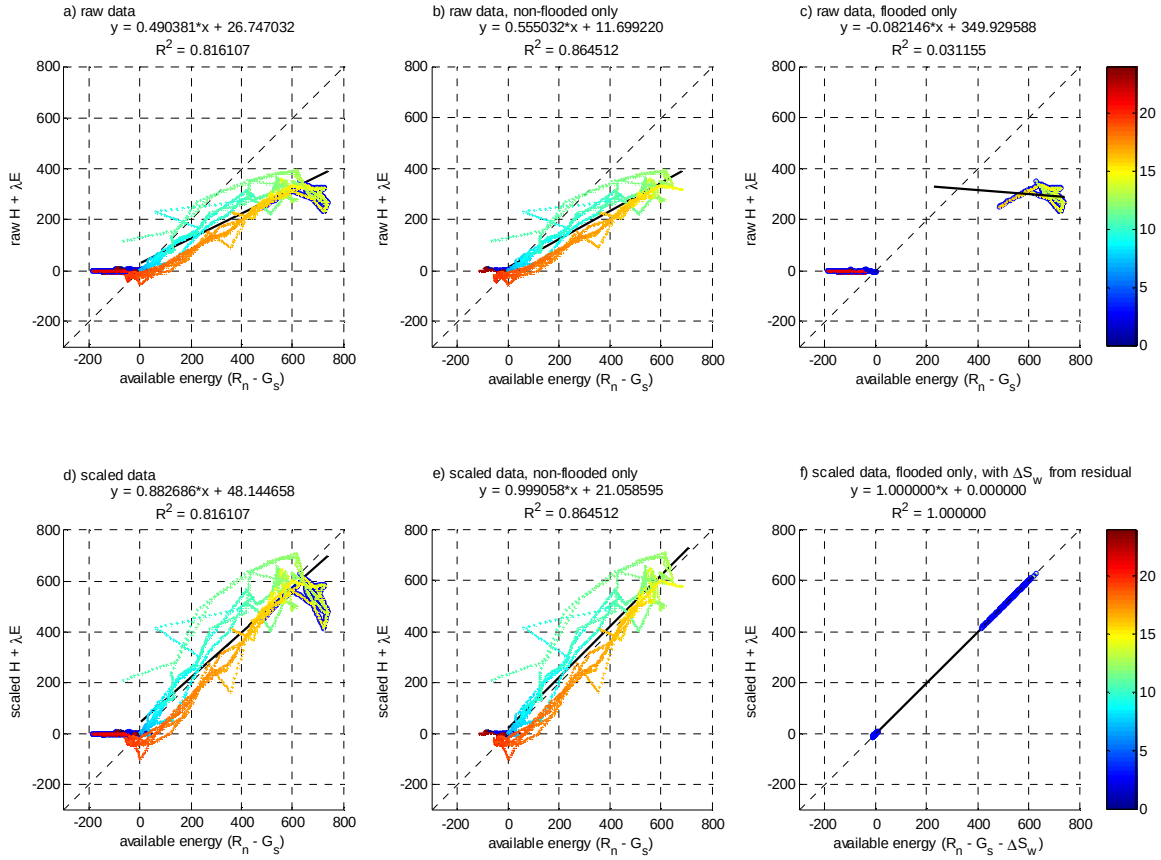

Figure S2. Illustration of energy balance closure. Complete energy balance closure is represented by the 1:1 line. Regressions, regression equations, and R^2 values are shown based on daytime data only. Data points are colored according to the hour of the day, starting from midnight.

4. Plant leaf gas flux measurements and details of leaf metabolism model

4.1 Biophysical parameters

The photosynthetically active radiation (*PAR*) incident on a plant, the availability of CO_2 gas and water to the plant, and the plant's enzymatic physiology combine to determine the rate at which photosynthesis can assimilate carbon into the plant (A). Crucially, the availability of CO_2 gas to the plant is controlled by the conductance of stomata to CO_2 (g_{sc}) in the plant leaf. The stomata permit CO_2 to diffuse into the leaf as photosynthesis draws down the concentration of CO_2 inside (C_i) the stomata below that of the ambient atmosphere. The H_2O vapor pressure in a stomata is very near saturation and so, unless the air is also saturated with water vapor, H_2O must concurrently diffuse out of the stomata (at a conductance g_{sw} proportional to g_{sc}) whenever CO_2 diffuses in: hence transpiration. To complicate matters, there are two types of leaf-level thermal feedback that occur and affect the rates of photosynthesis and transpiration. First, A depends on the leaf temperature, which leads to g_s being temperature dependent, but leaf temperature depends on the balance of H, λE and ΔS and λE depends on g_s: photosynthesis and transpiration are a coupled non-linear system. Second, leaf temperature determines a fraction of the long wave energy emitted from the earth surface and so affects the total radiation balance incident upon the canopy.

The leaf metabolism models we employed in this study are common in ecological and climatological applications. The coupled models [Collatz et al., 1991, 1992] combine the biochemical photosynthesis model of Farquhar et al. [1980] and the Ball-Berry stomatal conductance model [Ball, 1988]. The models are described in detail presently. We applied this leaf metabolism modeling method to two different scenarios representing vegetation of C_3 [Collatz et al., 1991] and C_4 [Collatz et al., 1992] photosynthetic types, the biophysical differences between which slightly alter the response of vegetation to changes in environmental conditions. Among major salt marsh plant species, only the grasses *Spartina* spp. and *Distichlis* spp. are C_4 plants; the balance of major salt marsh plants are of C_3 type, including the *Salicornia* spp., *Jaumea* spp., and *Grindelia* spp. found at our site [Drake, 1989].

These biophysical models require parameters related to plant metabolic rates that can be fit from eddy correlation data [Wolf et al., 2006] or estimated from controlled experiments on individual

plant leaves, the latter method used in this study. The biochemical parameters used in this study were estimated by taking leaf chamber measurements of net photosynthetic assimilation (A_n) at different light levels and CO_2 levels for leaves of the C4 grasses *Spartina foliosa* and *Distichlis spicata* and photosynthetic stems of the C3 succulent *Salicornia depressa*. The plants were taken from the field site with intact root systems in August 2008 (2-3 weeks prior to the field study and a few days before laboratory measurements), kept in an outdoor greenhouse under natural light, and watered periodically with bay water. Prior to measurement, the selected leaves/stems were wiped clean of salt with a damp cloth and allowed to air-dry. Leaf gas flux measurements (Licor LI-6400) were recorded once the fluxes had equilibrated to each change in light level, after 30-50 minutes.

Instrument [Licor LI-6400] settings for measurements on individual *Spartina* leaves used the measured leaf area (as a trapezoid with height 3 cm and bases equal to measured leaf widths at either end of the gas flux chamber) and a stomatal ratio of zero (to account for the lack of abaxial stomata in salt marsh *Spartina*). Multiple narrow *Distichlis* leaves were aligned in a single layer, in-parallel to enable a larger leaf measurement area; the leaf area was taken as the total spatial coverage of this multi-leaf arrangement; the stomtal ratio setting was 1, for stomtata on abaxial and adaxial sides. To take measurements on round *Salicornia* stems using the same flux chamber, a stem was selected of a length such that the succulent photosynthetic section could be coiled in a single layer in the chamber without breaking the stem; the woody portion of the stem below the photosynthetic section was aligned with the foam edge of the chamber and surrounded with a small bit of paraffin wax to enhance the seal of the flat chamber edges around the round stem; the leaf area was taken as one-half the stem surface area, estimated by treating the stem as a cylinder and measuring diameter and length; the stomatal ratio setting used for *Salicornia* was 1.

The CO_2 and light response curves were used with standard nonlinear curve-fitting software (Levenberg-Marquart algorithm) to find the biochemical parameters (V_m) that minimized the differences between the observations and the Collatz et al. [1991, 1992] models for C3 and C4 plants.

284 *4.2 Model architecture*

285 This following describes the calculations used to calculate the fluxes of CO_2 (net
286 assimilation) and H_2O vapor (transpiration) between the atmosphere and the interior of a leaf
287 during photosynthesis, as controlled by the leaf biochemistry and ambient conditions. The model
288 is solved iteratively since the system components are coupled: the net carbon assimilation
289 depends on internal CO_2 partial pressure inside the stomata, this partial pressure depends on the
290 total conductance, and the total conductance is regulated by the plant according to the rate of
291 carbon assimilation. The calculations are as in Collatz et al. [1991, 1992] unless otherwise noted.
292 See table S2 for variable and parameter definitions, units, values, and sources.
293
294 1) Define ambient conditions: T_a, S_d, RH, u, and P. Input LAI.
295 Calculate T_l, Q_p, w_a, and w_i.
296 $T_l = 0.59 \cdot T_a + 10.28$ (fit from laboratory data)
297 $Q_p = 0.46 \cdot 4.55 \cdot S_d \cdot (1 - \exp(-0.5 \cdot LAI))$
298 $w_a = \left((RH/100) \cdot e^*_{Ta}\right) / P$
299 $w_i = \left(e^*_{Tl}\right) / P$
300 $e^*_T = 1000 \cdot 0.6108 \cdot \exp\left(\frac{17.27 \cdot T}{T + 237.3}\right)$ [Allen et al. 1998, Tetens 1930]
301 2) Provide static inputs: leaf biophysical parameters (Table S2), C_{ca}, C_{oa}, d.
302 Calculate p_{oa}.
303 $p_{oa} = \left(C_{oa}/10^3\right) \cdot P$
304 3) Choose an initial guess for g_{sv}, e.g., 1 mol/m^{2}s [Collatz 1991, pg. 119].
305 Calculate g_{sc}, g_{bv}, g_{bc}, g_{tv}, g_{tc}.
306 $g_{sc} = g_{sv}/1.6$
307 $g_{bv} = 0.147\sqrt{u/d}$ [Campbell and Norman, 1998 (7.33)]
308 $g_{bv} = 0.110\sqrt{u/d}$ [Campbell and Norman, 1998 (7.33)]
309 $g_t^{-1} = g_s^{-1} + g_b^{-1}$
310 4) Choose initial guess for C_{ci}, e.g., $C_{ci} = 0.9 * C_{ca}$.
311 Calculate p_{ci}.

$$p_{ci} = \left(C_{ci}/10^6\right) \cdot P$$

5) Account for temperature-dependence of leaf biophysical parameters.

$$q_T = \left(T_l - 25\right)/10$$

$$R_d = \frac{R_{d,25} \cdot Q_{10,Rd}^{\ qT}}{1 + \exp\left(1.3 \cdot \left(T_l - 55\right)\right)} \quad \text{for} \quad R_{d,25} = R_{df} \cdot V_{m,25}$$

a) For a C3 plant:

$$K_c = K_{c,25} \cdot Q_{10,Kc}^{\ qT}$$

$$K_o = K_{o,25} \cdot Q_{10,Ko}^{\ qT}$$

$$\tau = \tau_{25} \cdot Q_{10,\tau}^{\ qT}$$

$$V_m = \frac{V_{m,25} \cdot Q_{10,Vm}^{\ qT}}{1 + \exp\left(\frac{-a_1 + a_2\left(T_l + 273\right)}{R\left(T_l + 273\right)}\right)}$$

b) For a C4 plant:

$$k = k_{25} \cdot Q_{10,k}^{\ qT}$$

$$V_m = \frac{V_{m,25} \cdot Q_{10,Vm}^{\ qT}}{\left(1 + \exp\left(0.3 \cdot \left(13 - T_l\right)\right)\right)\left(1 + \exp\left(0.3 \cdot \left(T_l - 36\right)\right)\right)}$$

6) Calculate the light compensation point, the CO_2 partial pressure at which A_n is zero.

$$\Gamma_* = \frac{p_{oa}}{2\tau}$$

7) Calculate the three possible assimilation rates.

a) For a C3 plant:

i) Light-limited:

$$J_E = \frac{\alpha_p \cdot e_m \cdot Q_p \cdot \left(C_{ci} - \Gamma^*\right)}{C_{ci} + 2 \cdot \Gamma^*}$$

ii) Rubisco (RuBP-carboxylase) regeneration-limited:

$$J_C = \frac{V_m \cdot \left(C_{ci} - \Gamma^*\right)}{C_{ci} + K_c \cdot \left(1 + C_{oa}/K_o\right)}$$

iii) Sucrose production-limited:

$$J_S = V_m/2$$

b) For a C4 plant:

i) Light-limited:

$$J_E = \alpha \cdot Q_p$$

ii) Rubisco (RuBP-carboxylase) regeneration-limited:

$$J_C = V_m$$

iii) Sucrose production-limited:

$$J_S = k \cdot p_{ci} / P$$

8) Account for co-limitation by finding the minimum assimilation rate using sequential quadratic approximations.

$$J_P = \frac{J_E + J_C - \sqrt{(J_E + J_C)^2 - 4\theta J_E J_C}}{2\theta}$$

$$A = \frac{J_P + J_S - \sqrt{(J_P + J_S)^2 - 4\beta J_P J_S}}{2\beta}$$

9) Subtract the daylight plant leaf respiration rate to calculate net assimilation.

$$A_n = A - R_d$$

10) Calculate a new estimate for C_{ci} based on this net assimilation rate, ambient CO_2 availability, and the total conductance between the air and the leaf interior according to a gradient-flux relationship.

$$C_{ci} = C_{ca} - A_n / g_{tc}$$

11) Iterate steps 4-10 until C_{ci} converges (e.g., until the difference between sequential C_{ci} calculations is < 0.001 μmol/mol).

12) Use the Ball-Berry empirical relationship to calculate a new estimate of g_{sv} based on A_n.

$$g_{sv} = m \frac{A_n h_s}{C_{cs}} + b$$ Ball-Berry stomatal conductance model

for:

$C_{cs} = C_{ca} - (A_n / g_{bc})$ CO_2 concentration at leaf surface

$E_{ti} = -g_{tv} \cdot (w_a - w_i)$ instantaneous transpiration E_{ti} (mol H_2O/m^2s)

$h_s = (w_a - (E/g_{bv}))/w_i$ humidity at leaf surface

13) Iterate steps 3-12 until g_{sv} converges (e.g., until the difference between sequential g_{sv} calculations is < 0.001 mol/m^{2}s).

14) Account for non-plant ecosystem respiration, R_{eco}, as a fraction of net production.

$$R_{eco} = -\beta_A \cdot A_n$$ with negative sign to indicate opposite direction from A_n

15) Calculate net ecosystem exchange (*NEE*).

$$NEE = A_n - R_{eco} = A_n(1-\beta_A)$$

16) The instantaneous molar leaf transpiration rate (*E*) is calculated again from the final (converged) estimate of g_{sv}, then converted to a latent heat flux estimate, then converted to units of latent heat flux.

λE (W/m^2) = E (mol H_2O /m^{2}s) * 2.45x10^6 (J/kg) * 0.001 (kg/g) * 18 (g/mol H_2O) = E_{ti} * 4.41 × 10^4

17) Account for non-plant evapotranspiration (soil evaporation). According to Beer's Law, the energy penetrating the plant canopy and so available for soil evaporation decreases exponentially according to the leaf area index (*LAI*).

$$soil\ evaporation\ \ factor = e^{-0.5 \cdot LAI}$$

With the parsimonious assumption that the transpiring canopy and wet soil evaporate at similar rates, we scale up the simulated canopy latent energy flux (λE) by the above factor to estimate the total evapotranspiration and latent heat flux.

$$\lambda E_{total} = \lambda E_{canopy} + \lambda E_{canopy}\left(\frac{e^{-0.5 \cdot LAI}}{1-e^{-0.5 \cdot LAI}}\right)$$

Table S2. Flux model variables, parameters, fixed parameter values, and units

Model Variable	Symbol	Value	Units	Source
ambient air temperature	T_a		°C	
incident shortwave solar radiation	S_d		W/m^2	
ambient air relative humidity	*RH*		%	
wind speed	u		m/s	
atmospheric pressure	P		Pa	
leaf temperature	T_l		°C	
photosynthetically active radiation (PAR) quantum flux density	Q_p		μmol/m^{2}s	
saturation vapor pressure at temperature T	e^*_T		Pa	
ambient air vapor pressure	e_a		Pa	
mole fraction of H_2O vapor in ambient air	w_a		--	
mole fraction of H_2O vapor in air inside leaf	w_i		--	
concentration of O_2 in ambient air	C_{oa}	210	mmol/mol	
partial pressure of ambient O_2	p_{oa}		Pa	

concentration of CO_2 in ambient air	C_{ca}	340	µmol/mol	
characteristic leaf dimension (width)	d	0.01	m	
stomatal conductance to H_2O vapor	g_{sv}		mol/m^{2}s	
stomatal conductance to CO_2	g_{sc}		mol/m^{2}s	
boundary layer conductance to H_2O vapor	g_{bv}		mol/m^{2}s	
boundary layer conductance to CO_2	g_{bc}		mol/m^{2}s	
total conductance to H_2O vapor	g_{tv}		mol/m^{2}s	
total conductance to CO_2	g_{tc}		mol/m^{2}s	
concentration of CO_2 in air inside leaf	C_{ci}		µmol/mol	
partial pressure of CO_2 in air inside leaf	p_{ci}		Pa	
humidity fraction at leaf surface	h_s		--	
net photosynthetic carbon assimilation	A_n		µmol/m^{2}s	
transpiration rate (instantaneous)	E_{0i}		mm/day	
Constant C3 model parameters				
Ball-Berry model intercept	b	0.01	mol/m^{2}s	c
maximum quantum efficiency: *a.k.a.*, intrinsic quantum yield	e_m	0.08	mol CO_2/mol PAR	c
leaf absorptivity of *PAR*	α_p	0.825	--	c
Michaelis constant for CO_2	$K_{c,25}$	30	Pa	a
temperature coefficient for K_c	$Q_{10,Kc}$	2.1	--	a
inhibition constant for O_2	$K_{o,25}$	30000	Pa	a
temperature coefficient for K_o	$Q_{10,Ko}$	1.2	--	a
temperature coefficient for V_m	$Q_{10,Vm}$	2.4	--	a
high-temperature V_m limitation factor 1	a_1	220000	J/mol	a
high-temperature V_m limitation factor 2	a_2	703	J/mol K	a
ideal gas constant	R	8.314472	J/mol K	a
day respiration factor	R_{df}	0.015	--	c
day respiration	$R_{d,25}$		µmol/m^{2}s	
temperature coefficient for R_d	$Q_{10,Rd}$	2.0	--	a
CO_2/O_2 specificity ratio	τ_{25}	2600	mmol/mmol	a
temperature coefficient for τ	q_τ	0.57	--	a
light/rubisco co-limitation factor	θ	0.95	--	c
(light/rubisco)/sucrose co-limitation factor	β	0.98	--	c
Calibrated C3 model parameters				
maximum Rubisco capacity, uncalibrated	$V_{m,25}$	100	µmol/m^{2}s	c
Ball-Berry model slope, uncalibrated	m	9	--	c
Constant C4 model parameters				
Ball-Berry model intercept	b	0.04	mol/m^{2}s	c
initial slope of photosynthetic light response	α	0.04	mol/m	b
initial slope of photosynthetic CO_2 response	k_{25}	0.7	mol/m^{2}s	b
temperature coefficient for k	$Q_{10,k}$	2	--	b
temperature coefficient for V_m	$Q_{10,Vm}$	2	--	b
day respiration factor	R_{df}	0.025	--	c
day respiration	$R_{d,25}$		µmol/m^{2}s	
temperature coefficient for R_d	$Q_{10,Rd}$	2.0	--	b
light/rubisco co-limitation factor	θ	0.95	--	c
(light/rubisco)/sucrose co-limitation factor	β	0.8	--	c

Calibrated C4 model parameters				
maximum Rubisco capacity, uncalibrated	$V_{m,25}$	30	μmol/m^{2}s	c
Ball-Berry model slope, uncalibrated	*m*	4	--	c

Sources: (a) Collatz et al. [1991], (b) Collatz et al. [1992], (c) Sellers et al. [1996] Table 5.

5. Detailed flux model results

Figures S3 and S4 illustrate the flux modeling results in comparison to the measured field data.

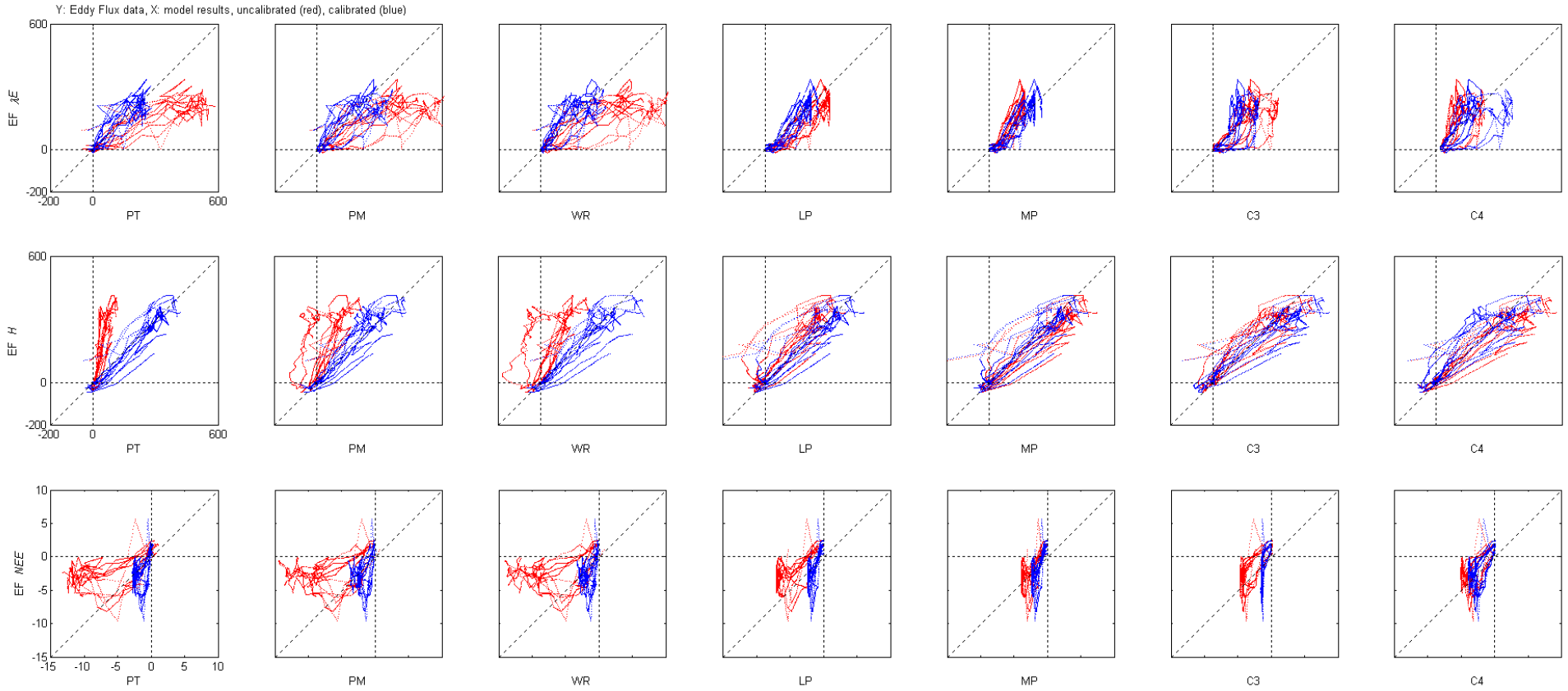

Figure S3. Scatter plots illustrating the correlation between the eddy flux field data (on y-axis) and simulation results (on x-axis). Uncalibrated simulation results are in red, calibrated simulation results are in blue. The axes and 1:1 line are shown for reference.

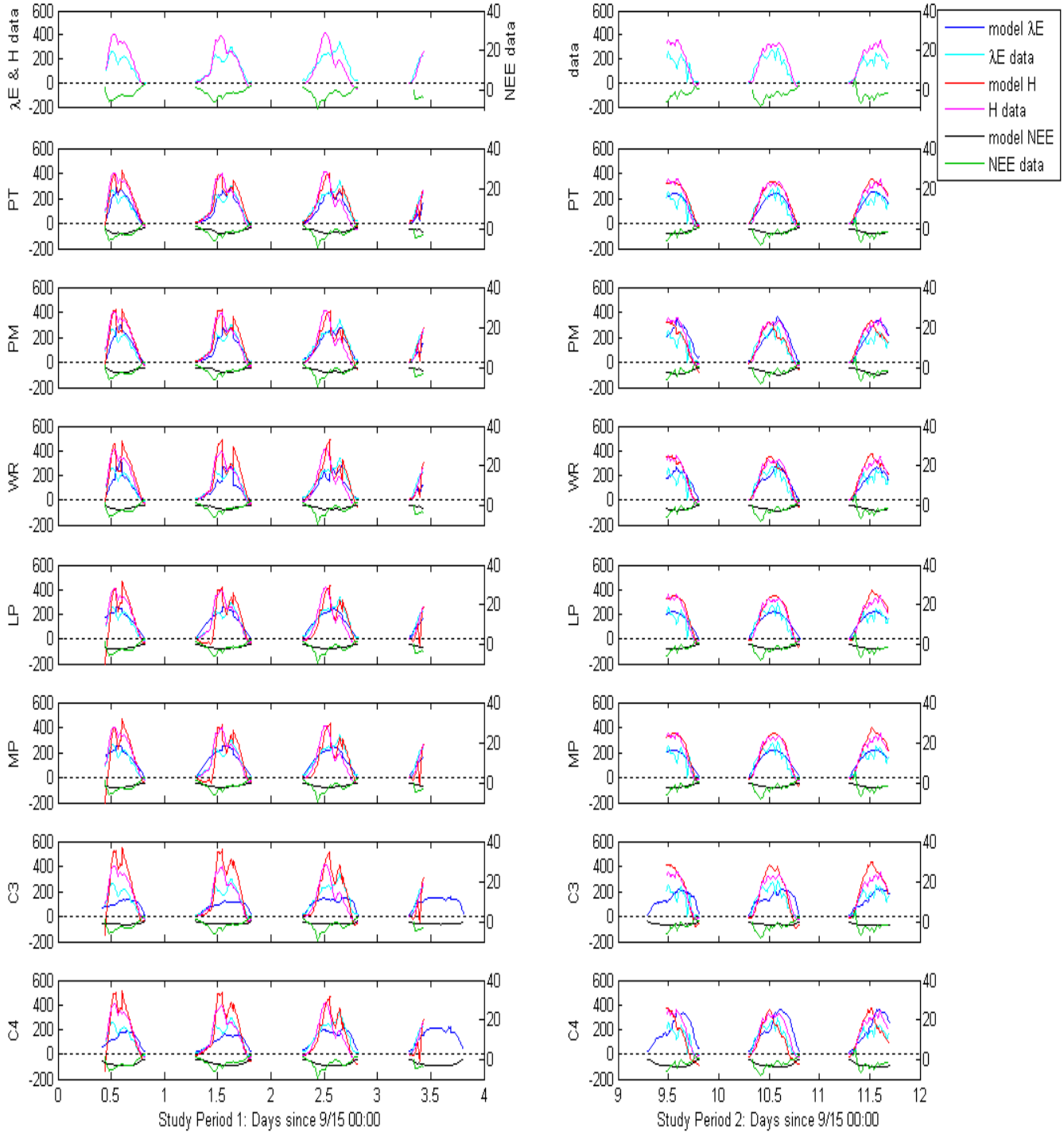

384

385 **Figure S4.** Calibrated model results in comparison to eddy flux data.

386 (C3 and C4 results shown are from calibration scenario 1, Table 6, of the manuscript.)

387

6. References cited in supplement

Ball, J. T. (1988), An analysis of stomatal conductance, Ph.D. thesis, Stanford University, Stanford, CA.

Collatz, G. J., J. T. Ball, C. Grivet, and J. A. Berry (1991), Physiological and environmental regulation of stomatal conductance, photosynthesis and transpiration: a model that includes a laminar boundary layer, *Agr. Forest Meteorol.*, *54*(2-4), 107-136.

Collatz, G. J., M. Ribas-Carbo, and J. A. Berry (1992), Coupled photosynthesis-stomatal conductance model for leaves of C_4 plants, *Aust. J. Plant Physiol.*, *19*(5), 519-538.

Drake, B. G. (1989), Photosynthesis of salt marsh species, *Aquat. Bot.*, *34*(1-3), 167-180.

Eugster, W., J. P. Mcfadden, and E. S. Chapin (1997), A comparative approach to regional variation in surface fluxes using mobile eddy correlation towers. Boundary *Bound.-Lay. Meteorol.*, *85*(2), 293-307.

Farquhar, G. D., S. von Caemmerer, and J. A. Berry (1980), A biochemical model of photosynthetic CO_2 assimilation in leaves of C_3 species, *Planta*, *149*(1), 78-90.

Lee, X.H., J. Finnigan, and K.T.P. U (2004), Coordinate systems and flux bias error, in *Handbook of Micrometeorology*, edited by X. H. Lee, W. J. Massman and B. Law, Kluwer, Dordrech.

Massman, W. J. (2000), A simple method for estimating frequency response corrections for eddy covariance systems. *Agr. Forest Meteorol.*, *104*(3), 185-198.

Shuttleworth, W. J. (1993), Evaporation, in *Handbook of Hydrology*, edited by D. R. Maidment, McGraw-Hill, New York.

Twine, T. E., W. P. Kustas, J. M. Norman, D. R. Cook, P. R. Houser, T. P. Meyers, J. H. Prueger, P. J. Starks, and M. L. Wesely (2000), Correcting eddy-covariance flux underestimates over a grassland, *Agr. Forest Meteorol.*, *103*(3), 279-300.

Webb, E. K., G. I. Pearman, and R. Leuning (1980), Correction of flux measurements for density effects due to heat and water-vapor transfer, Q. *J. Roy. Meteor. Soc*., *106*(447), 85-100.

Wolf, A., K. Akshalov, N. Saliendra, D. A. Johnson, and E. A. Laca (2006), Inverse estimation of Vc_{max}, leaf area index, and the Ball-Berry parameter from carbon and energy fluxes, *J. Geophys. Res.-Atmos.*, *111*, D08S08, doi:10.1029/2005JD005927.